Journal of Materials Chemistry A

ROYAL SOCIETY OF CHEMISTRY

PAPER

View Article Online
View Journal

Cite this: DOI: 10.1039/d0ta05298a

Affinity-engineered carbon nanofibers as a scaffold for Na metal anodes†

Alessandro Susca, Jiapeng Liu, Jiang Cui, Nauman Mubarak, Junxiong Wu, Muhammad Ihsan-Ul-Haq, Francesco Ciucci and Jang-Kyo Kim *

Received 25th May 2020
Accepted 6th July 2020

DOI: 10.1039/d0ta05298a

rsc.li/materials-a

Metal anodes possess the potential to disrupt the limits imposed by intercalation compounds and achieve a higher storage density for next-generation rechargeable batteries. This study is dedicated to engineering a scalable scaffold made of carbon nanofibers (CNFs) modified with embedded ZnO nanoparticles as facile nucleation sites for enhanced Na plating performance. The pristine CNF network provides a highly conductive, mechanically stable plating platform while the porous morphology effectively lowers the local current density and the volume fluctuations, delivering 1500 cycles at 1 mA cm^{-2}. In search of appropriate sodiophilic surface for stable Na plating, the affinities between Na and different substrate materials are analyzed by measuring overpotentials, coulombic efficiencies, and through density functional theory calculations. The ZnO@CNF composite created by *in situ* incorporation of ZnO nanoparticles offers uniform nucleation and deposition of Na through conversion and alloying reactions, leading to ameliorated cyclic stability at a high current density of 3 mA cm^{-2}. The Na plating thickness is predicted based on simple electrochemical principles and geometric considerations, corroborating experimental measurements. The affinity-engineered ZnO@CNF anodes deliver more than 1000 h of stable plating/stripping cycles in a symmetric battery configuration by effectively inhibiting the growth of dendrites and Na agglomerates.

Introduction

The issues arising from repeated plating and stripping of alkali metals, especially Li and Na, have made their application in energy storage highly challenging. Metallic Li is widely used in primary batteries because of its high specific energy,[1,2] and Na has been successfully applied in high-temperature Na/S devices for stationary applications.[3] However, the use of alkali metals in room-temperature rechargeable batteries has been limited to an intercalation or alloying-based chemistry since the release of the first Li-ion batteries almost three decades ago.[4,5] While such a chemistry ensures a high degree of stability by avoiding direct contact between the reactive alkali metal and the electrolyte, the practical specific capacities are much reduced from their theoretical values of 3860 mA h g^{-1} for Li and 1165 mA h g^{-1} for Na.[6,7] In particular, Na-based batteries are considered more viable for long-term mass production than their Li counterparts due to several techno-economic reasons.[8]

Abandoning any host material and using Na in its elemental state do not come without challenges. Similar to metallic Li,[9–11] the growth of dendrites during the electroplating of Na is known to be a key challenging issue.[12–14] Although the range of parameters influencing dendritic growth has yet to be fully understood due to the experimental difficulties of characterizing such a phenomenon, the underlying mechanism can be summarized in light of recent studies,[15–19] as follows. Metallic Na reacts with the liquid electrolyte creating a solid electrolyte interphase (SEI), whose composition and stability are highly dependent on both the solvent, the ionic salt and its concentration in the electrolyte.[15,16] Electrochemical plating causes the depositing Na to nucleate on a limited number of rough sites on the current collector, where the electric field is higher than the surrounding flat area. The large volume fluctuation arising from the newly deposited Na leads to the formation of narrow cracks in the SEI layer, through which Na grows uncontrollably into dendrite-shaped protuberances. Possible outcomes after prolonged growth of dendrites are then (i) perforation of the separator and consequent short circuit during plating, and (ii) detachment of the dendrites and formation of "dead Na", which is then entirely isolated from the circuit.[17] It can be concluded that an SEI layer with good chemical and mechanical stability can contain the growth of such an undesired dendrite structure.[18] The current density heavily influences the process, with a low current density allowing Na to nucleate densely on the surface.[19] Moreover, a low current density can decrease the probability of dendrite growth by avoiding large polarization and fast growth at the reaction front.[8]

Department of Mechanical and Aerospace Engineering, The Hong Kong University of Science and Technology, Clearwater Bay, Kowloon, Hong Kong. E-mail: mejkkim@ust.hk

† Electronic supplementary information (ESI) available. See DOI: 10.1039/d0ta05298a

Research on Li metal anodes pioneered the field of metal anodes, leading to significant progress in suppressing the growth of dendrites and achieving uniform plating/stripping.[6,20,21] Among several successful strategies, the current study is mainly concerned with the following approaches. (i) The first one involves developing a conductive and mechanically stable matrix possessing a large surface area. Such a structure is not only able to drastically reduce the local current density – an important parameter for dendritic growth – but also to contain and accommodate the volume expansion upon repeated cycles. (ii) The second approach is to enhance the affinity between the deposited alkali metal and current collector, resulting in reduced nucleation energy to the advantage of dense nucleation against uncontrolled growth. These two strategies were also combined together to develop a 3D conductive scaffold with high affinity nucleation sites, achieving outstanding results for Li metal batteries.[22–27] As for the Na counterpart, the benefits of high-affinity nucleation substrates have been proven in many studies, using a nanocarbon layer on an Al current collector,[28] a gold film sputtered on a Cu collector,[29] several different alloying metals[30] and even a layer of silk-derived pyroproteins.[31] 3D conductive networks such as carbon felt[32] and carbon microspheres,[33] porous copper[34] and aluminum[35] were also proven to be effective. The two strategies have been simultaneously applied with carbon nanotube electrodes containing N- and S-functional groups,[36] catalytic carbon nanotemplates,[37] and doped and porous carbon fibers[38,39] where the substrate surface condition ameliorated the affinity to Na.

In summary, a low growth rate is essential to achieve stable Na plating/stripping cycles. An electrode possessing a large specific surface area (SSA) lowers the growth rate by increasing the active contact area for plating. Dense and favorable Na nucleation reduces the growth rate by increasing the number of growing nuclei instead. Here we present such a synergic strategy to minimize the local current density and offer a large and favorable deposition surface through the use of a network of inexpensive carbon nanofibers (CNFs) whose morphology was engineered by incorporating myriads of sodiophilic zinc oxide nanoparticles (ZnO@CNFs). The rationale behind the choice of strategy is schematically illustrated in Fig. 1. ZnO@CNFs act not only as a current collector having high affinity and a large SSA, but also as a 3D scaffold to accommodate the plated Na. We prove that a pCNF network even without any additional materials attached had a beneficial effect due to its large SSA and high porosity while ZnO possessed a higher affinity to Na than other commonly used materials like Cu and Al. We subsequently present the superior performance of ZnO@CNFs as an affinity-engineered conductive scaffold.

Experimental

Fabrication of CNF films

CNFs were produced *via* electrospinning of a polymeric precursor, 5 wt% solution of polyacrylonitrile (PAN) in DMF. The precursor for ZnO@CNFs was prepared by adding 7.5 wt% of $ZnAc_2$ into the neat PAN solution. The zinc salt was dehydrated overnight in a vacuum oven at 135 °C before adding into the solution. The precursor solutions were electrospun at a voltage of 18 kV and a pump rate of 1 mL h^{-1} on a rotating collector drum. The freshly spun fibers were stabilized in an oven at 230 °C for 3.5 h in air, and carbonized in a tube furnace at different temperatures ranging from 650 to 800 °C for 1 h in a nitrogen atmosphere, with a temperature ramp of 2 °C min^{-1}. The resulting CNF film was then cut into disk shapes of 14 mm in diameter before being used as an electrode.

Substrates for affinity studies

Cu, Al, Mg and Zn were introduced as freestanding foils; Ag, Al_2O_3 and SiO_2 were thermally evaporated on Cu foil; Pt, Ag and carbon were sputtered on Cu foil; Sn was deposited on Cu foil as

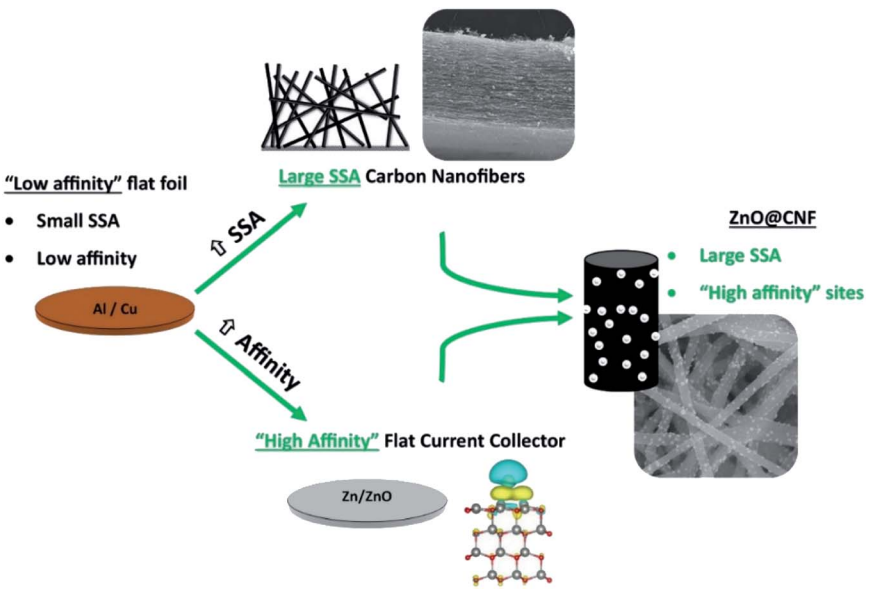

Fig. 1 Schematic of the synergetic rationale behind the ZnO@CNF electrode design.

a surface film from the high temperature decomposition of tin(II) acetate; ZnO was produced by oxidizing zinc foil at 300 °C for 10 h.

Materials characterization

The synthesized materials were examined by SEM (JSM-6700F, JEOL) and TEM (JEM 2010, JEOL). No conductive coating was applied to any of these materials before electron microscopy. The powder XRD analysis (PW1830, Philips) was carried out on flat current collectors, pCNFs and ZnO@CNFs at 2θ ranging between 10 and 80°. The thermogravimetric analysis (TGA, Q5000, TA Instruments) was performed in a nitrogen atmosphere from room temperature to 800 °C, with a heating ramp of 10 °C min^{-1} up to 600 °C, and of 2 °C min^{-1} from 600 °C to 800 °C. The sheet resistance of CNF films was measured on a Hall effect measurement system (Ecopia HMS-5500). The surface functionality was investigated with XPS (Axis Ultra DLD, Kratos Analytical). The nitrogen adsorption/desorption isotherms were obtained on an automated adsorption apparatus (Micromeritics, ASAP 2020) to measure the BET surface area and porosity.

Electrochemical characterization

All electrochemical tests were conducted using CR2032 coin cells assembled in an Ar-filled glovebox. The different cell setups are shown in Fig. S1.† Half cells were prepared using the CNF film as a freestanding working electrode without adding a current collector, and Na foil as reference and counter electrodes. All electrodes for CE tests were cut into discs of 14 mm in diameter for working electrodes and 16 mm for counter electrodes. Overpotentials were measured based on the same half-cell configuration, but using the said substrates as working electrodes. For symmetric cells, ZnO@CNFs was stacked on top of Na foil and served as both working and counter electrodes. The control cells were prepared using a pure Na foil as both working and counter electrodes. All electrodes for symmetric cells were cut into discs of 14 mm in diameter. The electrolyte was prepared from 1 M $NaCF_3SO_3$ in diglyme for all experiments, except for the carbonate-electrolyte cells where the electrolyte was prepared using 1 M $NaClO_4$ in EC : PC (1 : 1). 80 μL of electrolyte was typically used. A single polymeric separator (Celgard 2400) was used for all experiments, except for the carbonate-electrolyte cells where a glass fiber separator (Whatman GF/D) was used after cutting into discs of 18 mm in diameter. Electrochemical impedance spectroscopy (EIS) measurements were conducted of symmetric cells with frequencies ranging from 10.0 mHz to 100 kHz.

Results and discussion

Na plating on pCNFs with a large surface area

A network-like current collector possessing a good electrical conductivity, a large SSA and stable mechanical properties is a likely candidate to suppress dendritic growth and enable uniform Na plating and stripping during repeated cycles. Carbon nanomaterials are an obvious choice to satisfy such requirements, thanks to their highly tunable morphology and intrinsic electrical and mechanical properties.[40,41] Since the choice of Na over Li is dictated mainly by economic consideration, it follows then that the choice of the current conductor should also consider price and availability as key factors. Electrospun CNFs are relatively inexpensive, easy to process and viable to scaling-up to an industrial scale.[42,43] Moreover, the produced CNF current collectors are freestanding and do not require an additional binder or metallic foil for use as electrodes.

The CNF network was realized by electrospinning of a polyacrylonitrile (PAN) precursor dissolved in dimethylformamide (DMF). The material and process parameters of electrospinning were carefully controlled to obtain a flexible film of ~100 μm in thickness after carbonization. While the performance of CNFs carbonized at different temperatures was very similar at a low current density of 1 mA cm^{-2}, the difference in cyclability became considerable with increasing current density (Fig. S2†), probably due to the different electrical conductivities of the different samples. The electrical conductivity was measured to be 4.0×10^{-4}, 3.6×10^{-2} and 1.6 S m^{-1} for the samples carbonized at 650, 725 and 800 °C, respectively. After extensive trial and error, 800 °C was chosen as the carbonization temperature in this study. The CNFs after carbonization were randomly dispersed and 100–150 nm in diameter, as shown in Fig. 2a and S3.† The X-ray diffraction (XRD) pattern confirms that the carbon in the fibers was mostly amorphous (Fig. S3†), as expected from the low carbonization temperature of 800 °C.[44] The Brunauer–Emmett–Teller (BET) surface area of the CNF film measured using a nitrogen adsorption/desorption test was 16.9 m^2 g^{-1}.

The electrochemical performance of neat CNF anodes was evaluated in a half-cell configuration *versus* pure Na, see the cell schematics presented in Fig. S1.† A single layer of polymer separator, Celgard 2400, was used to maintain the experiment close to practically scalable conditions. It is assumed that the use of multiple layers or of thick separators would unrealistically delay the battery failure, when that happens by a dendrite-induced short circuit. The *ex situ* SEM image of CNFs taken after Na plating at 1 mA cm^{-2} presented a moderate degree of Na agglomeration especially at the fiber junctions, with small agglomerates dispersed along the fiber length, as shown in Fig. 2b. This observation indicates that the CNF film functioned as a current collector with a large SSA effectively reducing the local current density during the deposition of Na. The coulombic efficiency (CE) in a half-cell configuration is a measure of available plated Na, and a stable CE signifies uniform and reversible plating and stripping. The CE of the CNF network as a freestanding anode is compared with the one using a flat carbon-coated Cu current collector at a current density of 1 mA cm^{-2}, as shown in Fig. 2c. The CNF current collector was cycled for almost 1600 full cycles with a very stable average CE of over 99.6%, whereas the latter metal current collector exhibited highly fluctuating CEs even from the first cycle and an overall life of less than 400 cycles before experiencing a short circuit. The capacity–voltage curves of the first 10 cycles are shown in Fig. 2d and e for the flat carbon current

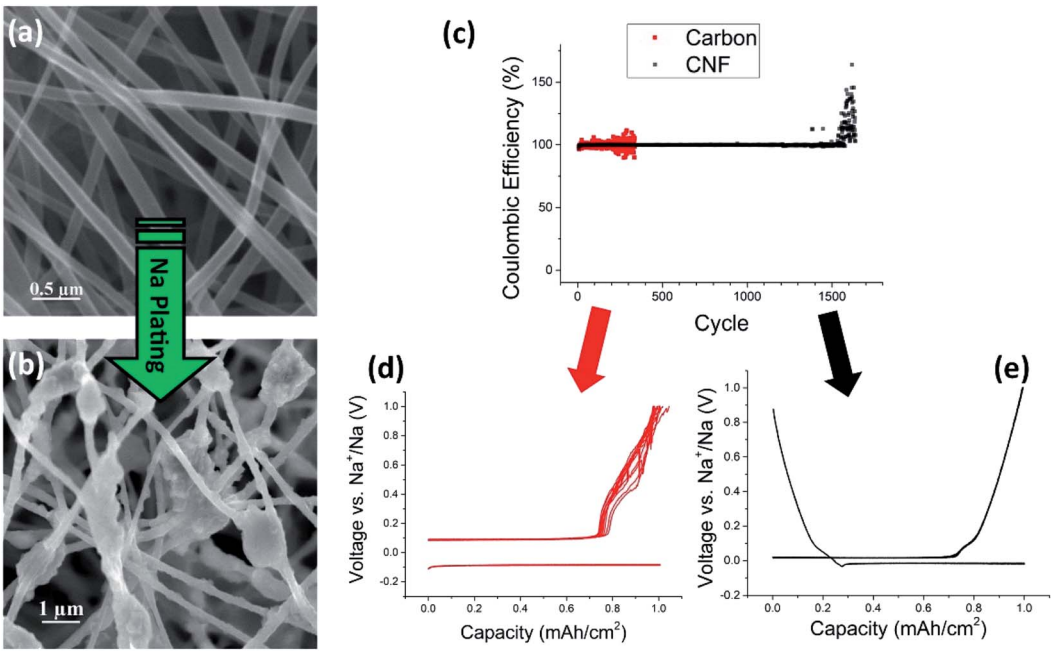

Fig. 2 SEM images of CNF network (a) before and (b) after Na deposition with a loading of 0.15 mA h cm^{-2}. (c) Coulombic efficiencies of flat carbon and CNF network electrodes measured using a half cell configuration against Na at a loading of 1 mA h cm^{-2} and a current density of 1 mA h cm^{-2}. Voltage variations in the first 10 plating/stripping cycles of Na on (d) a flat carbon current collector and (e) a CNF network, measured at a current density of 1 mA h cm^{-2}.

collector and the CNF respectively, highlighting several chaotic voltage peaks during stripping of the flat metal current collector and a contrasting stable voltage profile of the 3D fiber network. In the case of flat carbon, only the plating curve (negative voltage) and the stripping curve with chaotic peaks were detected. Essentially the same behavior as the flat carbon is shown in Fig. S4† for a flat Cu current collector without a carbon coating. For the CNF electrode, brief Na insertion and extraction portions appear before plating and after stripping, respectively.

To understand how the increasing SSA could slow the Na growth during plating, the thickness of deposited Na on the two different current collectors was estimated. The surface area of a flat disk-shaped current collector was 1.54 cm^2. Based on the typical areal loading of the CNF electrode and its Brunauer–Emmett–Teller (BET) surface area, the total surface area of one CNF current collector was estimated to be ~254 cm^2, which is 165 times larger than the flat counterpart. For example, assuming an ideal case in which plating happens uniformly on all the available surface, a 10 μm thick layer plated on the flat current collector would be redistributed through the whole CNF network to obtain only about 60 nm thick plating. The fast and large volumetric increase of Na on a flat current collector is thus likely to result in the formation of dendrites with a rough morphology. These can perforate the separator during plating or lose contact with the current collector during stripping, as suggested by the chaotic voltage profile during charging (Fig. 2d), leading respectively to a short circuit or to a permanent loss of capacity.

The current density is among the main factors influencing the stability of an alkali-metal battery in a long term cyclic experiment, showing a sharp decrease in lifetime with increasing current density for both Li[45,46] and Na storage.[47,48] To understand the performance of our materials at their limiting current, the half-cell cyclic tests were performed at a higher current density of 3 mA cm^{-2} with an increased loading of 3 mA h cm^{-2}. The long-term cyclic behavior at this current was severely destabilized as seen from the CE results in Fig. S1.† The best CNF cell survived less than 300 stable cycles, after which an irreversible capacity loss prevailed. It appears that even the large SSA of the CNF electrode was unable to lower the local plating rate at such a high current density. It follows then that the nucleation of Na had to be ameliorated by enhancing the Na-affinity of the fibers.

Na plating on substrates with different affinities

Nucleation, the first step during deposition, requires a relatively high energy for the creation of an interface between Na and the substrate. When depositing at a constant current density, a temporary overpotential is needed to provide the first nucleation energy, whose magnitude is dictated by how difficult the interfacial relaxation is. The mechanism behind the plating behavior is summarized in Fig. 3a. This observation means that the deposition overpotential can represent the affinity between the two materials. Such a strategy has already been widely implemented for Li[26,49–51] and Na,[27–29,35] showing that a reduced overpotential led to a denser nucleation during deposition. In an effort to identify favorable species, the overpotentials of a wide range of materials, including Cu, Al, Al_2O_3, SiO_2, Au, Ag, Pt, Mg, Sn, Zn and ZnO, were evaluated at a low current of 30 μA. The initial overpotential was found only if the substrate was

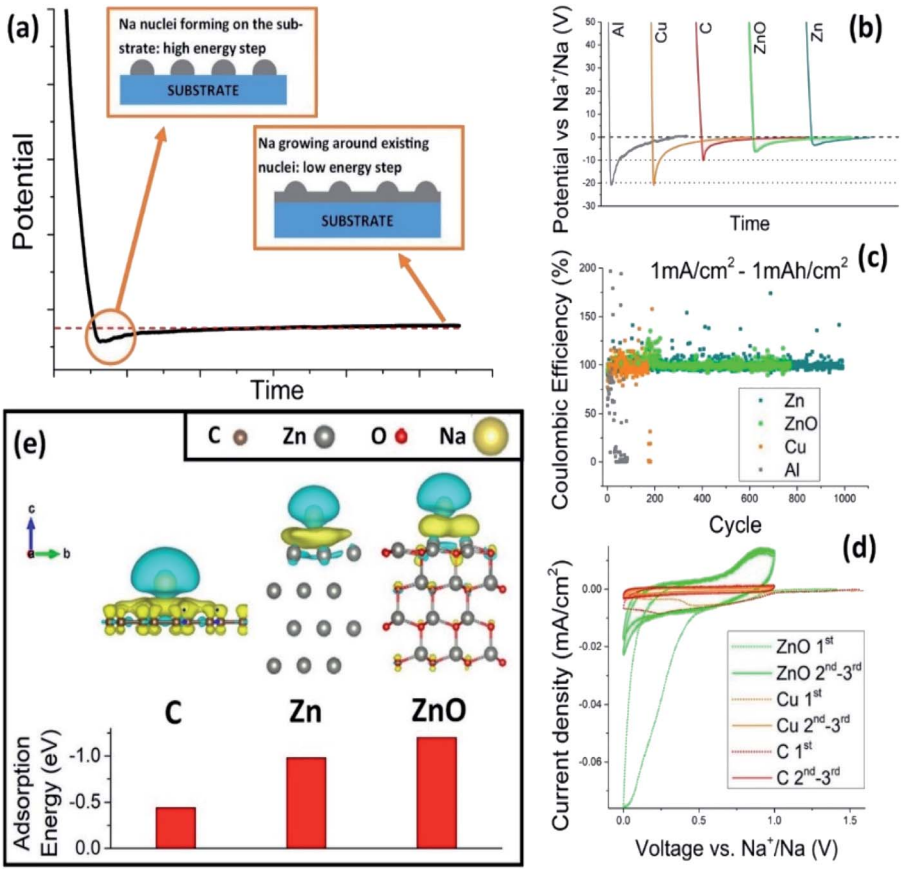

Fig. 3 (a) Typical voltage profile of Na deposition highlighting two steps with an overpotential in the first nucleation step and steady state low voltage in the second growth step; (b) voltage changes *vs.* Na^+/Na over time for Na deposition on different substrates at a constant current of 30 μA; (c) coulombic efficiencies of different substrates measured during repeated charge/discharge cycles at 1 mA cm^{-2} in a half-cell configuration; (d) cyclic voltammetry of half cells with ZnO and Cu *vs.* Na^+/Na between 0 and 1 V at a scan rate of 0.1 mV s^{-1}, where the dashed lines correspond to the first cycle and the solid lines to the second and third cycles. (e) Electron density differences of Na adsorption on carbon, Zn and ZnO according to the DFT calculations and their adsorption energy.

previously completely stripped of any residual Na, while partial stripping led to a zero-overpotential plating (Fig. S5†). This confirmed that the overpotential was indeed directly related to the creation of a new interface. Moreover, for some selected materials, the overpotential method was corroborated by the evaluation of CE values and the *ab initio* calculation of adsorption energies.

The overpotential values for the different substrates are summarized in Table 1. The voltage behaviors over time showing the overpotential differences are given in Fig. 3b for several different materials. Similar data for all other substrate materials are shown in Fig. S6.† It is important to notice that none of these materials had a zero-overpotential interaction with Na, as opposed to Li which is known to have high affinity with several metal substrates, such as Au.[26] Among them, Zn and Sn exhibited the lowest overpotentials of 4 and 3 mV, respectively, for Na deposition, followed by ZnO and Au both with 7 mV. In contrast, a very high overpotential of 20 mV was necessary to deposit Na on Cu and Al. Previously, Au Sn and Zn were found to have high affinity for Na nucleation.[28,29,52]

The coulombic efficiencies of Zn and ZnO current collectors upon repeated Na plating/stripping cycles are shown in Fig. 3c in comparison with those of Cu and Al. It is important to note that the flat metal current collectors with a small surface area were subjected to a relatively high local current density and

Table 1 Overpotentials of different metals for deposition of Na, measured at a constant current of 30 μA in a half-cell configuration. Overpotentials were approximated to the closest unit according to the experimental accuracy

Materials	Overpotential [mV]
Cu	20
Al	20
SiO_2	11
Carbon	10
Al_2O_3	10
Ag	10
Mg	10
Pt	10
Au	7
ZnO	7
Sn	4
Zn	3

their CEs were not as stable as for the 3D CNF counterparts. In fact, the *ex situ* SEM image in Fig. S7† shows that Na deposition on a Zn plate was predominantly of dendritic nature, similar to that on Cu. However, while such a structure on a Cu plate tended to vertically accumulate to form mountain-like deposits (see later discussion on Fig. 5a and b), the dendrites deposited on a flat Zn plate were dispersed throughout the whole electrode surface. Hence, the chance to lose contact with the collector and generate "dead Na" would be low. Consequently, there were few irreversible capacity losses for over 1000 cycles for Zn and for over 800 cycles for ZnO, whereas the capacity loss became evident within the first few cycles for Al and in less than 200 cycles for Cu.

Density functional theory (DFT) was explored to quantify the adsorption energies of Na on the said substrates. Vienna *ab initio* simulation package (VASP) was used to simulate the interaction between Na and carbon, Zn, ZnO, and Sn. The calculation results indicate that Na adsorbs more favorably on the (0001) surface of ZnO or Zn than on the pure carbon surface. The adsorption energies of Na were −1.20, −0.98 and −0.44 eV on ZnO (0001), Zn (0001) and carbon, respectively, confirming better affinity of Na with the former two substrates than the latter. Fig. 3e shows the plot of the electron density differences obtained from the calculations. According to the electrochemical measurements, Sn exhibited the lowest deposition overpotential which corroborates with the high adsorption energy of −1.25 eV for the Sn (001) surface, the highest value among all substrates studied here. More information on the DFT calculations can be found in Note S1, along with Fig. S8 and S9.†

Cyclic voltammetry (CV) was employed to investigate the interaction between Na and the current collectors at different voltages, as shown in Fig. 3d. While carbon presented a slightly larger hysteresis than Cu, ZnO was the only material showing major reaction peaks. A broad anodic peak was noted at 1 V, descending almost close to 0 V, and a cathodic peak appeared between 0.75 and 1.0 V. This finding is consistent with previous reports on ZnO for Na-ion batteries.[53–55] Previous *in situ* studies proposed a two-step reaction:

$$ZnO + 2Na^+ + 2e^- \rightarrow Zn + Na_2O \quad (1)$$

$$xZn + Na \rightarrow NaZn_x \quad (2)$$

where $x = 13$ for a full alloying reaction.[56,57] The cited studies identified all phases given in eqn (1) and (2) using *in situ* transmission electron microscopy (TEM) and selected area (electron) diffraction (SAED) analysis of ZnO nanowires during their sodiation. The $NaZn_{13}$ phase could not be detected using the *ex situ* XRD analysis in this study, because its thickness failed to generate a strong signal. However, the reaction (1) of ZnO with Na was detected by the *ex situ* XRD analysis, as shown in Fig. S10.† The same ZnO substrate was characterized before and after discharge to 5 mV, and the results signified a large increase in metallic Zn signal after the electrochemical process, a reflection of ZnO converting to metallic Zn. Zn could then alloy with Na upon plating, facilitating the nucleation on the substrate.[26,29] Prominent peaks of Na_2O, a product of the proposed reaction between ZnO and Na, were also noted from the XRD pattern. Moreover, the current density in the CV experiment sharply increased when the ZnO cell approached 0 V: at 1 mV, the current density for ZnO was 12 and 7.5 times higher than the ones for Cu and carbon, respectively. Such a sharp increase was associated with the lower deposition overpotential of Na on ZnO, enabling it to be plated at a higher voltage than on less sodiophilic surfaces.

ZnO@CNFs with enhanced Na affinity

One of the main advantages of electrospun nanofibers is their tunable properties, where incorporating different types of materials at the precursor level can *in situ* insert desired effects.[58–61] Dehydrated zinc acetate ($ZnAc_2$) was added to the PAN/DMF precursor solution to obtain a final product with high-affinity ZnO nanoparticles embedded in the fibers. Although metallic Sn and Zn appeared to be the best choices in terms of overpotential, incorporating them in the nanoscale fibers was found to be highly challenging. Both elemental Sn and Zn are present in the liquid state at the temperature necessary for carbonizing the electrospun nanofibers,[62] hence these metals tended to severely agglomerate. Thus, we have chosen ZnO nanoparticles to incorporate in CNFs in this study. The freshly electrospun fibers were stabilized at 220 °C in air before final carbonization: after stabilization $ZnAc_2$ was found decomposed into ZnO (XRD pattern in Fig. S11†). The rationale behind the optimization of the processing parameters is reported in Note S2, along with Fig. S12–S14:† a ratio of $ZnAc_2$ to PAN of 3 : 2 was chosen, along with a carbonization temperature of 725 °C.

The ZnO@CNFs maintained a similar average diameter to the pCNFs (~150 nm), and contained ZnO nanoparticles of 30–40 nm in diameter uniformly dispersed within and on the surface of fibers, as shown in Fig. 4a and S15.† The SAED patterns and the high-resolution TEM (HRTEM) images confirmed the hexagonal phase of ZnO (Fig. 4b). The electrical conductivity was 5×10^{-2} S m^{-1} while the BET surface area was measured to be 7.1 m^2 g^{-1}, which is much smaller than that of the pCNFs due to the higher density of fibers containing ZnO particles. The overall ZnO@CNF film thickness was ~100 μm. High resolution X-ray photoelectron spectroscopy (XPS, Fig. S16†) was used to probe the surface chemistry of CNFs with and without ZnO. Zn 2p and Zn LMM peaks at binding energies of 1021.9 and 498.1 eV were evidence of the presence of ZnO in ZnO@CNFs. The deconvoluted carbon 1s peak was very similar for both pCNFs and ZnO@CNFs, suggesting that the addition of ZnO did not cause significant changes in the carbon surface functionalization. In order to investigate the internal distribution of ZnO nanoparticles, the fiber film was decomposed in air at 700 °C to obtain residual ZnO. The residual film was characterized by an interconnected network of ZnO nanoparticles (Fig. S17†) whose diameters were slightly larger than those within the fiber, indicating that the ZnO particles were uniformly dispersed within the fiber network and coalesced during the decomposition of the carbon matrix. The

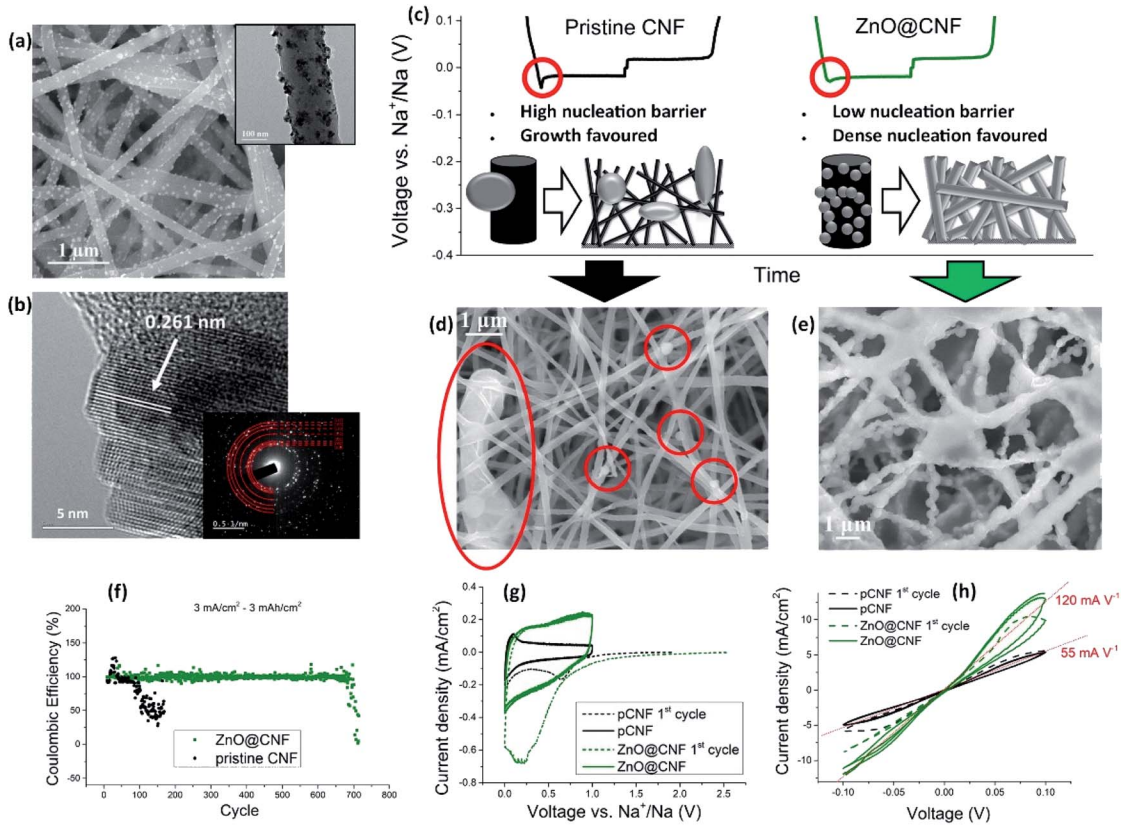

Fig. 4 (a) SEM and TEM (inset) images of ZnO@CNFs; (b) HRTEM image and SAED (inset) of a ZnO nanoparticle embedded in ZnO@CNFs. *d*-spacing and reflection planes are highlighted. (c) Typical voltage profiles of a plating/stripping cycle for the pristine CNF and ZnO@CNF cells, highlighting the difference in overpotential and illustrating its implications; (d and e) SEM images of pCNFs and ZnO@CNFs, respectively, after discharge to 0 V *versus* metallic Na. (f) Coulombic efficiencies of the pCNF and ZnO@CNF half cells with a loading of 3 mA h cm^{-2}, measured at a current density of 3 mA cm^{-2}; (g) cyclic voltammetry of half cells made from pCNFs and ZnO@CNFs at a scan rate of 0.1 mV s^{-1} where the first cycle is represented by a dashed line; (h) cyclic voltammetry of symmetric cells made from pCNFs and ZnO@CNFs at a scan rate of 0.1 mV s^{-1} where the first cycle for both materials is represented by a dashed line, while the second and third cycles by solid lines, and the red lines signify the linear fits and the corresponding slopes.

morphology of the ZnO@CNF electrode was examined by *ex situ* SEM after 200 plating/stripping cycles, exhibiting a structurally durable electrode with intact fiber networks and attached ZnO particles (Fig. S18†). The performance of the material was then evaluated through three stages: Na nucleation and its implication, Na plating behavior, and the long-term stability after Na infusion.

Electrochemical performance of ZnO@CNF electrodes. Fig. 4c shows the typical plating/stripping voltage profiles of the pCNF and ZnO@CNF electrodes and explains how the increased affinity ameliorated the Na deposition by increasing the nucleation density over the fiber network. The effectively reduced overpotential of the ZnO@CNF electrode meant electrochemically active ZnO nanoparticles with high sodiophilicity. The activity of the ZnO nanoparticles could also be signaled by the increase in discharge capacity in the range between 1 and 0 V, respectively from 190 to 300 μA h cm^{-2} for pCNFs and ZnO@CNFs. Fig. 4d and e present *ex situ* SEM images of pCNFs and ZnO@CNFs respectively, after a first discharge to 0 V. Under these discharge conditions, the nucleation of Na already started occurring, as suggested by the negative growth of current in the CV curves (Fig. 4g). Only an initial part of nuclei appeared at a voltage above 0 V, leaving most of the fibers still "naked", thus providing explicit visualization of the difference in nucleation density. The majority of pCNFs were uncovered with few nuclei and random agglomerates appearing in the network, see the larger overview of the same sample in Fig. S19.† Most nucleation occurred at the fiber junctions, a similar observation to previous reports for Li.[21] In contrast, the ZnO@CNF electrode exhibited a large number of nuclei under the same conditions, which covered almost the entire CNF network.

The beneficial effect of increased nucleation density could be proven by the stable coulombic efficiency of the ZnO@CNF electrode during long-term cycles at 3 mA cm^{-2} and 3 mA h cm^{-2} (Fig. 4f): ZnO@CNFs survived up to 700 stable cycles. Although the CE did not reach 100% as reliably as when testing at a lower current, the tested cells showed a significant delay in irreversible capacity loss compared to the pCNF electrode. The performance of the electrode is compared to the current state-of-the-art counterparts in Table S1.† The ZnO@CNF performance at a high current of 3 mA cm^{-2} and

a high capacity of 3 mA h cm^{-2} with 700 stable cycles, which corresponds roughly to 1600 h of testing, is among the best and hardly matched by any reported materials. Similar to the results obtained for a flat ZnO current collector, a conversion reaction was detected *via* XRD and CV analysis. The XRD pattern of the ZnO@CNFs discharged to 5 mV lost the characteristic ZnO reflections and some of the Zn and Na_2O peaks are now visible, as shown in Fig. S11.† Fig. 4g presents the CV curves for half cells with pCNF and ZnO@CNF electrodes during the first three cycles. The ZnO@CNF electrodes exhibited a broad anodic peak at ~1 V and a cathodic peak at above 0.75 V, corresponding to the conversion reactions previously described. These peaks were absent for the pCNF electrode. The current density at a voltage of 1 mV was more than twice as high for ZnO@CNFs than for pCNFs, signifying much favored plating in the former electrode. The CV curves obtained using symmetric cells at voltages ranging between −0.1 and 0.1 V are shown in Fig. 4h. The voltage–current slopes were over twice as large for ZnO@CNFs than for pCNFs, *i.e.* 120 *versus* 55 mA V^{-1} for linear fits after the first cycle, confirming a much lower resistance to plate for the ZnO@CNF electrode than the latter. Electrochemical impedance spectroscopy (EIS) was also employed to corroborate the claimed stability of the ZnO@CNF electrode. No large changes in impedance parameters were detected in the first 100 cycles at 3 mA cm^{-2}, suggesting marginal degradation of electrode or electrolyte consumption upon cycles (Fig. S20 and Table S2†). Furthermore, while the measurements reported here were tested with a glyme-based electrolyte, a steep improvement in electrochemical performance was detected even with a commercial carbonate electrolyte, as reported in Note S3 and Fig. S21.†

Plating behavior of ZnO@CNF electrodes. *Ex situ* microscopy was used to investigate how the different nucleation behavior would influence the final plating homogeneity. Fig. 5 presents the SEM images taken at different magnifications of a flat Cu collector, pCNF and ZnO@CNF electrodes after plating of the same amount of Na at different current densities. In the following is the summary of the observations made from the SEM images, comparing the Na deposition behavior of the three different current collectors.

(1) The flat Cu foil current collector possessed a small SSA and low affinity to Na, resulting in a high local current density and a high resistance to nucleation. Fig. 5a and b show that Na tended to deposit vertically to accumulate into mountain-like structures regardless of the current density, signifying that Na grew preferentially on the previously deposited sites instead of nucleating at new sites. The final micro-morphology exhibited needle-shaped structures of Na dendrites at both currents.

(2) pCNFs had a large SSA due to their 3D network, but low affinity to Na. Thus, the local current density was low, but nucleation was not favored along the fiber length. Na was efficiently incorporated into the scaffold at a low current density, as shown in Fig. 5c. Moderately sparse Na nuclei were seen, indicating that the nucleation density was high enough to ensure the containment of Na growth at a low current density because of the large surface area. However, at a higher current density, Na grew uncontrollably to form large agglomerates – so-called "islands" – on the fiber film surface, as shown in Fig. 5d and S22.† These protuberant structures developed vertically from the film, similarly to the mountain-like structures observed on the Cu foil. Microscopically, a small amount of plated Na was revealed in the fiber network and most of Na was present in the form of "islands". The intense Na signal over F signal in the energy dispersive X-ray spectroscopy (EDS) elemental map of these agglomerates (Fig. S23†) indicates that the "islands" could be formed by the dry electrolyte salt, confirming that they were

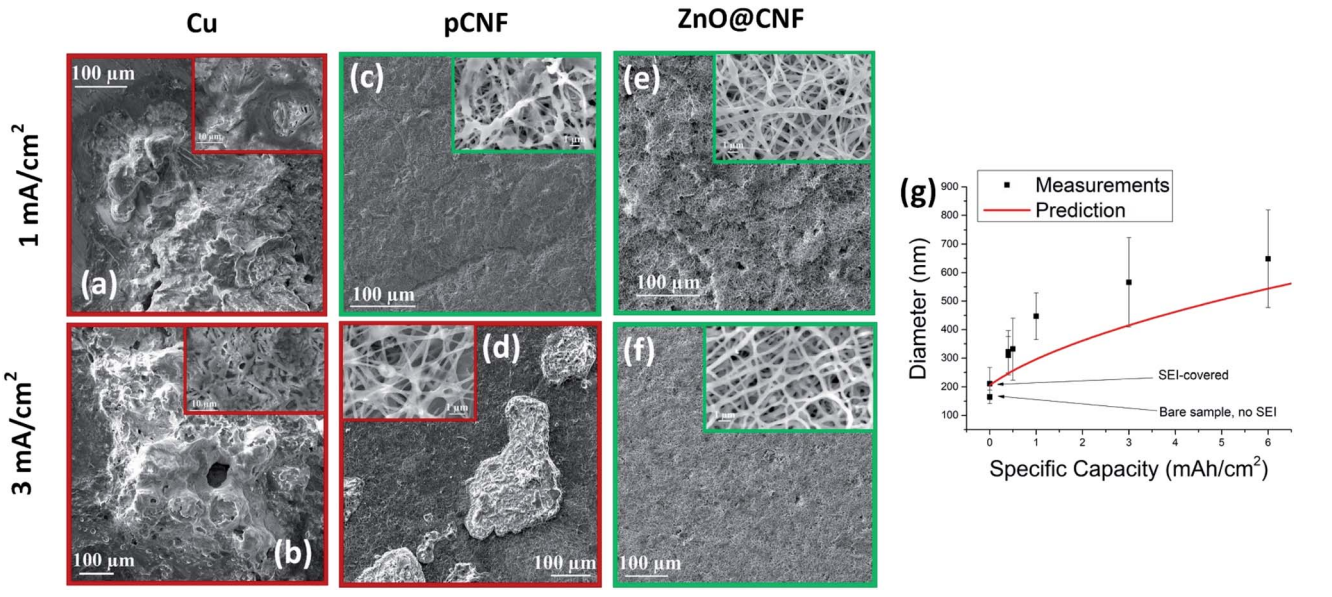

Fig. 5 SEM images of Na plated on a Cu current collector (a and b), pCNFs (c and d) and ZnO@CNFs (e and f) taken at low and high magnifications (insets). The current densities used are 1 mA cm^{-2} for (a, c and e), and 3 mA cm^{-2} for (b, d and f). The Na loading is 0.4 mA h cm^{-2} in all cases. (g) Comparison of fiber diameter between the experimental measurements using *ex situ* SEM images and the prediction from eqn (3).

indeed deposited Na. The EDS map of the area where no "island" was seen highlighted the presence of additional Na agglomerated below the electrode surface, as seen in Fig. S24.†

(3) ZnO@CNFs had a large SSA and a large number of high-affinity ZnO particles on the fiber surface. As such, the local current density was low, and the nucleation of Na on the whole fiber surface was favored. Fig. 5e and f confirm that the Na growth took place within the fiber network at both low and high current densities, and no macroscopic agglomeration was observed. The inset images present a quite uniform increase in fiber diameter from 100–150 to 250–300 nm after plating, proving a uniform Na layer was plated on the whole fiber network at both low and high current densities. The EDS elemental maps (Fig. S24†) support the above finding with little agglomeration compared to pCNFs.

Moreover, a thorough study of *ex situ* SEM images revealed that the gradual increase in fiber diameter caused by Na plating was reproducible and varied depending on the capacity of plated Na, as shown in Fig. S25.† This observation was unique to ZnO@CNFs and was not observed with pCNFs where Na grew in the form of agglomerates. To establish the correlation between the increase in fiber diameter and the applied charge, we formulated a model based on a simple electrochemical principle and geometric consideration. According to the details described in Note S4,† the diameter of ZnO@CNFs after Na plating can be written as a function of the plated capacity and is given by eqn (3):

$$D_{\text{prediction}} = \sqrt{\frac{4Q}{\pi LF}\frac{M_{\text{Na}}}{\rho_{\text{Na}}} + {d_0}^2} + t_{\text{SEI}} \quad (3)$$

where Q is the charge (in coulomb) applied during plating; L is the total length of the fiber network; F is the Faraday constant; M_{Na} is the molar mass of Na and ρ_{Na} is its density; d_0 is the diameter of the bare ZnO@CNF fibers; and t_{SEI} is the correction factor representing the increase in diameter after complete Na stripping, which is attributed to the SEI layer. The prediction is compared with the average diameters measured using magnified *ex situ* SEM images following Na plating under different charging conditions (Fig. S25†). Moderate accordance between the two was revealed, as shown in Fig. 5g, further suggesting a high degree of uniform Na plating on ZnO@CNFs. Interestingly, the measured diameters were found independent of applied current density, namely 1 or 3 mA h cm^{-2}, when the applied charge was identical, see Fig. S25-2 *vs.* Fig. S25-3.†

Long-term cyclic stability of symmetric cells. One of the most promising applications of metal anodes is to combine them with a sulfur or air cathode with a high energy density.[6,20] It is thus important to find an efficient way of infusing the alkali metal inside the anode scaffold. To introduce Na in the network, the anode was pre-assembled by stacking the CNF film on top of a pure Na foil. The Na foil was manually pressed into a thickness ranging between 200 and 400 μm. The use of this stacked design saved materials and processing time better than the classical sacrificial-cell electrodeposition method. The thickness of Na foil could be further reduced using industrial pressing tools. Fig. 6a presents a schematic of the stacking scheme of the assembled electrode which allowed Na to be effectively stripped and plated by removal and re-infiltration into the fiber network. Fig. 6b presents a side view of the CNF

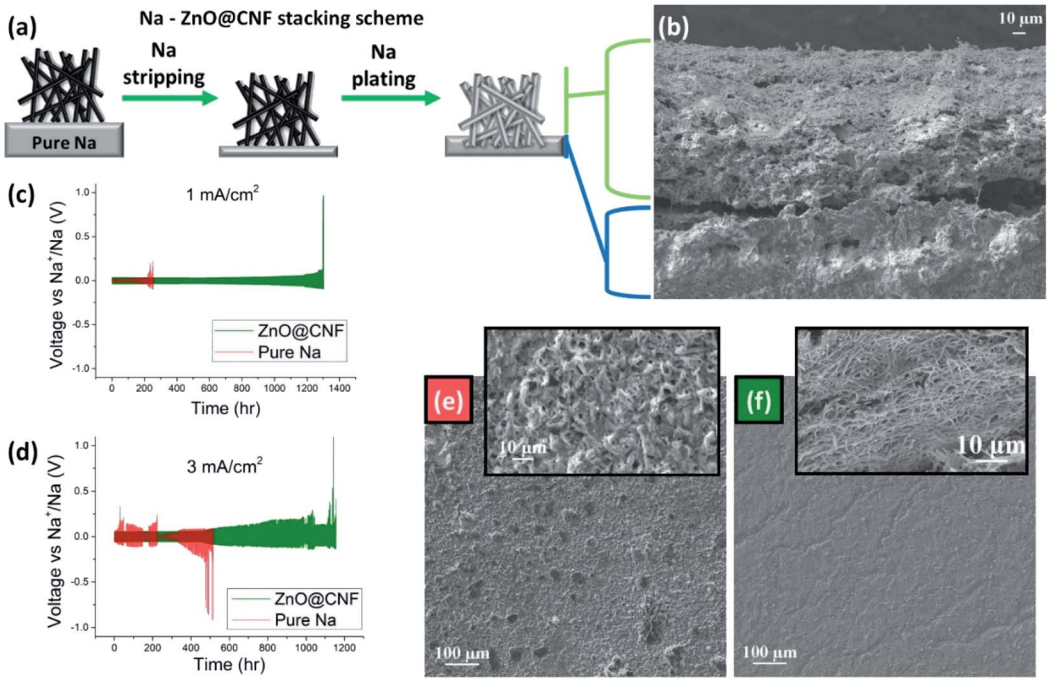

Fig. 6 (a) Schematics of the stacking of a pure Na film and ZnO@CNFs by network infusion when assembling symmetric cells. (b) Side view of the electrode after stripping followed by plating, highlighting the pure Na residual film (blue) and the layer of Na-infused fibers (green). (c and d) Cyclic performance of neat Na and ZnO@CNF symmetric cells measured at 1 and 3 mA cm^{-2}, respectively. The Na loading is 1 mA h cm^{-2} for both cases. (e and f) SEM images of the neat Na and ZnO@CNF symmetric cells after 40 cycles at 1 mA cm^{-2}, respectively.

film stacked on top of a Na layer after 6 mA h cm^{-2} of Na was stripped and re-deposited at a current density of 1 mA cm^{-2}. The image signifies successful re-infiltration of Na in the fiber network after the two-step process. The fiber diameter increased to ~600–800 nm from the initial ~150 nm, proving a large load of deposited Na. The final fiber thickness obtained with the stacked design was compatible with the thickness obtained with regular electrodeposition, indicating that a majority of Na was infiltrated from the initial film into the network. In view of the large variation in the measured Na thicknesses, however, it may be possible that some part of Na had been redeposited back onto the original Na film, as shown in the schematics. The above fiber network was likely to hinder any dendritic growth resulting from this scenario. The overall ZNO@CNF film thickness remained at ~100 μm after infiltration, suggesting that the network could withstand the mechanical pressure inside of the cell while retaining its original shape. The smooth top view of the same anode shown in Fig. S26† indicates that the ZnO@CNF film was able to hold and control the deposited Na even with a high areal loading of 6 mA h cm^{-2}.

Symmetric CNF–CNF cells (Fig. S1c†) were assembled by stacking the Na–ZnO@CNF anodes using the aforementioned infusion method. Symmetric Na–Na cells (Fig. S1b†) were also assembled for comparison. The voltage profiles of symmetric cells prepared at different current densities of 1 and 3 mA cm^{-2} with a fixed Na areal loading of 1 mA h cm^{-2} are shown in Fig. 6c and d, respectively. The pure Na cells survived about 200 h of stable plating/stripping cycles before showing the first short circuit at 1 mA cm^{-2} and even poorer performance at a higher current density. In contrast, the ZnO@CNF symmetric cells were able to endure more than 1000 h of cycles at both current densities without major voltage spikes. The importance of current density as a major factor influencing dendrite formation and cell failure was also highlighted by these findings. The neat Na cells in a symmetric configuration were found to endure a surprisingly long cycle life of 1000 h at a reduced current density of 0.5 mA cm^{-2}, see Fig. S27,† but they failed immediately after several cycles at a higher current density of 3 mA cm^{-2}.

Ex situ microscopy was used to link the electrochemical performance to the electrode plating behavior, as shown in Fig. 6e and f. Both cells were subjected to 40 cycles at 1 mA cm^{-2} before taking the SEM images. The neat Na electrode presents a very rough and porous surface. The characteristic needle-like dendritic structures with a thick layer (~100 μm) of highly porous re-deposited Na was noticed upon closer examination, see Fig. 6e. Fig. 6f presents the surface morphology of the ZnO@CNF cell showing a smooth surface free from any trace of dendrites, proving that the deposited Na was efficiently contained within the fiber network. The ZnO@CNF electrode retained the initial thickness of ~100 μm after 40 cycles (Fig. S28†), suggesting that the mechanical properties of the structure remained stable even after repeated plating/stripping cycles.

Conclusions

The network of CNFs was explored as a scaffold for stable plating and stripping of Na for Na metal batteries in this work. The following can be highlighted from the experimental studies combined with theoretical calculations:

(1) A CNF network with a large SSA was fabricated, and its use as a 3D current collector for the plating of metallic Na was studied. The large SSA was found to achieve much improved cyclic stability for a maximum of 1600 cycles at 1 mA cm^{-2} when compared to a flat carbon current collector.

(2) The affinity between Na and different substrates was analyzed by measuring overpotentials, CEs, and by DFT calculations. The results from these methods suggest that several metals, including Zn and ZnO, could offer a better plating surface than pure carbon. The reaction of Na with ZnO foil was studied and related to previous *in situ* studies.

(3) ZnO@CNF networks with embedded ZnO nanoparticles were fabricated with the addition of a zinc precursor before the electrospinning of fibers. The electrochemical measurements of overpotentials, cyclic voltammetry and SEM images during the first nucleation confirmed that the ZnO nanoparticles integrated in the CNF network acted as preferential plating sites. Consequentially, the ZnO@CNF electrode achieved a much longer cycle life than the pCNF counterpart.

(4) *Ex situ* microscopy was used to relate the improved nucleation behavior to the final plating homogeneity: while Na was plated with a poor morphology on a flat Cu current collector at both 1 and 3 mA cm^{-2}, pCNFs and ZnO@CNFs could distribute the Na loading on a large active surface area. Whereas Na agglomeration was found on the pCNF network, the improved nucleation behavior of ZnO@CNFs resulted in uniform plating at both low and high current densities.

(5) The thickness of Na layer plated on CNFs under these uniform deposition conditions was predicted based on simple electrochemical principles and geometric considerations, which reasonably agreed with experimental measurements using *ex situ* SEM images. This work appears to be the first attempt to estimate plating thickness on a porous nanofiber scaffold of metal batteries. The simple model formulated in this study is universal and can be applied to predict plating thickness in different metal batteries having other electrode structures like flat and particle shapes.

(6) Symmetric cells were fabricated using the Na-infused ZnO@CNF electrodes to study the long-term cyclic stability. Cells with ZnO@CNF electrodes survived more than 1000 h of plating/stripping cycles at both 1 and 3 mA cm^{-2}, whereas pure Na cells suffered short circuits much earlier in less than 200 h.

Conflicts of interest

There are no conflicts to declare.

Acknowledgements

This project was financially supported by the Innovation and Technology Commission (ITS/001/17) and the Research Grants Council (GRF Projects 16208718) of Hong Kong SAR. A. S. was a recipient of the Hong Kong PhD Fellowship. The authors also appreciate the technical assistance from the Materials

Characterization and Preparation Facilities (MCPF) and the Advanced Engineering Materials Facilities (AEMF) of HKUST.

Notes and references

1 C. A. Vincent, *Solid State Ionics*, 2000, **134**, 159.
2 B. Scrosati, *J. Solid State Electrochem.*, 2011, **15**, 1623.
3 Z. Wen, Y. Hu, X. Wu, J. Han and Z. Gu, *Adv. Funct. Mater.*, 2013, **23**, 1005.
4 M. Armand and J. M. Tarascon, *Nature*, 2008, **451**, 652.
5 J. B. Goodenough and K. Park, *J. Am. Chem. Soc.*, 2013, **135**, 1167.
6 D. Lin, Y. Liu and Y. Cui, *Nat. Nanotechnol.*, 2017, **12**, 194.
7 L. Ma, J. Cui, S. Yao, X. Liu, Y. Luo, X. Shen and J. K. Kim, *Energy Storage Mater.*, 2020, **27**, 522.
8 B. Lee, E. Paek, D. Mitlin and S. W. Lee, *Chem. Rev.*, 2019, **119**, 5416.
9 C. T. Love, O. A. Baturina and K. E. Swider-Lyons, *ECS Electrochem. Lett.*, 2014, **4**, A24.
10 Y. Ren, Y. Shen, Y. Lin and C. W. Nan, *Electrochem. Commun.*, 2015, **57**, 27.
11 J. Steiger, G. Richter, M. Wenk, D. Kramer and R. Mönig, *Electrochem. Commun.*, 2015, **50**, 11.
12 X. Zheng, C. Bommier, W. Luo, L. Jiang, Y. Hao and Y. Huang, *Energy Storage Mater.*, 2019, **16**, 6.
13 L. Fan and X. Li, *Nano Energy*, 2018, **53**, 630.
14 Y. Zhao, K. R. Adair and X. Sun, *Energy Environ. Sci.*, 2018, **11**, 2673.
15 R. Cao, K. Mishra, X. Li, J. Qian, M. H. Engelhard, M. E. Bowden, K. S. Han, K. T. Mueller, W. A. Henderson and J. G. Zhang, *Nano Energy*, 2016, **30**, 825.
16 J. Zheng, S. Chen, W. Zhao, J. Song, M. H. Engelhard and J. Zhang, *ACS Energy Lett.*, 2018, **3**, 315–321.
17 Y. Yui, M. Hayashi and J. Nakamura, *Sci. Rep.*, 2016, **6**, 22406.
18 W. Luo, C. F. Lin, O. Zhao, M. Noked, Y. Zhang, G. W. Rubloff and L. Hu, *Adv. Energy Mater.*, 2017, **7**, 1601526.
19 P. M. Bayley, N. M. Trease and C. P. Grey, *J. Am. Chem. Soc.*, 2016, **138**, 1955.
20 W. Xu, J. Wang, F. Ding, X. Chen, E. Nasybulin, Y. Zhang and J. Zhang, *Energy Environ. Sci.*, 2014, **7**, 513.
21 X. B. Cheng, R. Zhang, C. Z. Zhao and Q. Zhang, *Chem. Rev.*, 2017, **117**, 10403.
22 J. Cui, S. Yao, M. Ihsan-Ul-Haq, J. Wu and J. K. Kim, *Adv. Energy Mater.*, 2019, **9**, 1802777.
23 Y. Feng, C. Zhang, B. Li, S. Xiong and J. Song, *J. Mater. Chem. A*, 2019, **7**, 6090.
24 G. Huang, J. Han, F. Zhang, Z. Wang, H. Kashani, K. Watanabe and M. Chen, *Adv. Mater.*, 2019, **31**, 1805334.
25 Y. Zhou, K. Zhao, Y. Han, Z. Sun, H. Zhang, L. Xu, Y. Ma and Y. Chen, *J. Mater. Chem. A*, 2019, **7**, 5712.
26 Q. Dong, B. Hong, S. Hong, H. Fan, C. Gao and Y. Lai, *Electrochim. Acta*, 2018, **284**, 376.
27 K. Yan, Z. Lu, H. Lee, F. Xiong, P. Hsu, Y. Li, J. Zhao, S. Chu and Y. Cui, *Nat. Energy*, 2016, **1**, 16010.
28 A. P. Cohn, N. Muralidharan, R. Carter, K. Share and C. L. Pint, *Nano Lett.*, 2017, **17**, 1296.
29 S. Tang, Z. Qiu, X. Y. Wang, W. W. Wang, Y. Gu, X. G. Zhang, J. W. Yan, M. S. Zheng, Q. F. Dong and B. W. Mao, *Nano Energy*, 2018, **48**, 101.
30 S. Tang, Y. Y. Zhang, X. G. Zhang, J. T. Li, X. Y. Wang, J. W. Yan, D. Y. Wu, M. S. Zheng, Q. F. Dong and B. W. Mao, *Adv. Mater.*, 2019, **31**, 1807495.
31 M. E. Lee, H. W. Kwak, J. H. Kwak, H. J. Jin and Y. S. Yun, *ACS Appl. Mater. Interfaces*, 2019, **11**, 12401.
32 S. Chi, X. Qi, Y. Hu and L. Fan, *Adv. Energy Mater.*, 2018, **8**, 1702764.
33 H. Ye, C. Y. Wang, P. F. Wang, P. Wang, T. T. Zuo, Y. X. Yin, Z. J. Zheng, J. Cheng, F. F. Cao and Y. G. Guo, *Nano Energy*, 2018, **48**, 369.
34 T. S. Wang, Y. Liu, Y. X. Lu, Y. S. Hu and L. Z. Fan, *Energy Storage Mater.*, 2018, **15**, 274.
35 S. Liu, S. Tang, X. Zhang, A. Wang, Q. H. Yang and J. Luo, *Nano Lett.*, 2017, **17**, 5862.
36 B. Sun, P. Li, J. Zhang, D. Wang, P. Munroe, C. Wang, P. H. L. Notten and G. Wang, *Adv. Mater.*, 2018, **30**, 1801334.
37 H. J. Yoon, N. R. Kim, H. J. Jin and Y. S. Yun, *Adv. Energy Mater.*, 2018, **8**, 1701261.
38 Z. Zheng, X. Zeng, H. Ye, F. Cao and Z. Wang, *ACS Appl. Mater. Interfaces*, 2018, **10**, 30417.
39 N. Mubarak, M. Ihsan-Ul-Haq, H. Huang, J. Cui, S. Yao, A. Susca, J. Wu, M. Y. Wang, X. Zhang, B. Huang and J. K. Kim, *J. Mater. Chem. A*, 2020, **8**, 10269.
40 H. Ye, S. Xin, Y. X. Yin and Y. G. Guo, *Adv. Energy Mater.*, 2017, **7**, 1700530.
41 C. Zhang, Z. Huang, W. Lv, Q. Yun, F. Kang and Q. H. Yang, *Carbon*, 2017, **123**, 744.
42 A. G. MacDiarmid, W. E. Jones, I. D. Norris, J. Gao, A. T. Johnson, N. J. Pinto, J. Hone, B. Han, F. K. Ko, H. Okuzaki and M. Llaguno, *Synth. Met.*, 2001, **119**, 27.
43 B. Zhang, F. Kang, J. M. Tarascon and J. K. Kim, *Prog. Mater. Sci.*, 2016, **76**, 319.
44 B. Zhang, Y. Yu, Z. L. Xu, S. Abouali, M. Akbari, Y. B. He, F. Kang and J. K. Kim, *Adv. Energy Mater.*, 2014, **4**, 1301448.
45 Q. Li, S. Zhu and Y. Lu, *Adv. Funct. Mater.*, 2017, **27**, 1606422.
46 S. Choudhury and L. A. Archer, *Adv. Electron. Mater.*, 2016, **2**, 1500246.
47 S. Chi, X. Qi, Y. Hu and L. Fan, *Adv. Energy Mater.*, 2018, **8**, 1702764.
48 S. Tang, Z. Qiu, X. Y. Wang, W. W. Wang, Y. Gu, X. G. Zhang, J. W. Yan, M. S. Zheng, Q. F. Dong and B. W. Mao, *Nano Energy*, 2018, **48**, 101.
49 A. Pei, G. Zheng, F. Shi, Y. Li and Y. Cui, *Nano Lett.*, 2017, **17**, 1132.
50 C. Yang, Y. Yao, S. He, H. Xie, E. Hitz and L. Hu, *Adv. Mater.*, 2017, **29**, 1702714.
51 R. Zhang, X. R. Chen, X. Chen, X. B. Cheng, X. Q. Zhang, C. Yan and Q. Zhang, *Angew. Chem., Int. Ed.*, 2017, **56**, 7764.
52 T. Yang, T. Qian, Y. Sun, J. Zhong, F. Rosei and C. Yan, *Nano Lett.*, 2019, **19**, 7827.
53 Y. Teng, M. Mo, Y. Li, J. Xue and H. Zhao, *J. Alloys Compd.*, 2018, **744**, 712.
54 S. Sinha, P. N. Didwal, D. K. Nandi, J. Y. Cho, S. H. Kim, C. J. Park and J. Heo, *Ceram. Int.*, 2019, **45**, 1084.

55 M. Jing, F. Li, M. Chen, F. Long and T. Wu, *Appl. Surf. Sci.*, 2019, **463**, 986.
56 F. Xu, Z. Li, L. Wu, Q. Meng, H. L. Xin, J. Sun, L. Sun, B. Ge and Y. Zhu, *Nano Energy*, 2016, **30**, 771.
57 H. Asayesh-Ardakani, W. Yao, Y. Yuan, A. Nie, K. Amine, J. Lu and R. Shahbazian-Yassar, *Small Methods*, 2017, **1**, 1700202.
58 Y. Yu, L. Gu, C. Wang, A. Dhanabalan, P. Van Aken and J. Maier, *Angew. Chem., Int. Ed.*, 2009, **48**, 6485.
59 B. Zhang, Y. Yu, Z. Huang, Y. B. He, D. Jang, W. S. Yoon, Y. W. Mai, F. Kang and J. K. Kim, *Energy Environ. Sci.*, 2012, **5**, 9895.
60 F. Zhang, C. Yuan, J. Zhu, J. Wang, X. Zhang and X. W. Lou, *Adv. Funct. Mater.*, 2013, **23**, 3909.
61 Z. L. Xu, S. Yao, J. Cui, L. M. Zhou and J. K. Kim, *Energy Storage Mater.*, 2017, **8**, 10.
62 W. M. Haynes, *CRC Handbook of Chemistry and Physics*, CRC Press, 92nd edn, 2011.

